

pubs.acs.org/acscatalysis Research Article

Biogenic Manganese Oxide Synthesized by a Marine Bacterial Multicopper Oxidase MnxG Reveals Oxygen Evolution Activity

Wen Fu, Forrest P. Hyler, Joel Sanchez, Thomas F. Jaramillo, Jesús M. Velázquez, Lizhi Tao,* and R. David Britt*



Cite This: ACS Catal. 2024, 14, 7232-7242



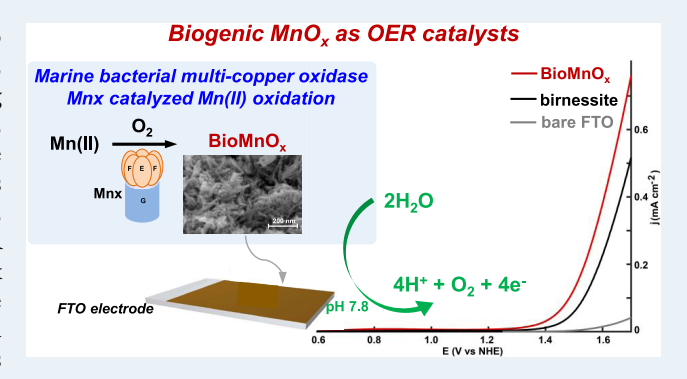
ACCESS I

III Metrics & More

Article Recommendations

s Supporting Information

ABSTRACT: Solar energy provides one major pathway to addressing global energy issues. Inspired by photosynthesis, nonbiological solar energy systems are designed for both absorbing light and "splitting water" to generate hydrogen fuel. However, during this process, the oxygen evolution reaction (OER) at the anode has a high kinetic barrier and overpotential, which reduces the overall efficiency. To improve the efficiency of the OER, significant efforts have been made to develop promising OER catalysts. Inspired by the highly efficient oxygen-evolving complex (OEC) in photosystem II in nature, manganese-oxide catalysts have garnered significant attention due to their low cost and minimal toxicity. However, the synthesis of most manganese-oxide catalysts requires strong oxidants, external high electric potentials, or highly



basic conditions, which make large-scale production energy-consuming and less efficient. In this study, we present a natural and clean process for synthesizing manganese-oxide catalysts by using an oceanic bacterial manganese oxidase named MnxG. The biogenic manganese oxides, as generated under different conditions, have different morphologies and crystalline structures and are as effective as or even more effective than synthetic birnessite. Spectroscopic analyses, including XANES, XPS, and EPR, suggest that the monoclinic-birnessite component, together with the surface Mn(III) species, plays a crucial role in the OER activity of biogenic MnO_x. This work provides insights into the development of efficient OER catalysts that can be produced by using a gentle and sustainable process.

KEYWORDS: biogenic manganese oxides, marine bacterial multicopper oxidase MnxG, oxygen evolution reaction (OER), electron paramagnetic resonance (EPR), manganese-oxide OER catalysts, water oxidation, X-ray photoelectron spectroscopy (XPS), X-ray absorption near-edge structure (XANES)

1. INTRODUCTION

Clean and affordable renewable energy sources are crucial to reducing our reliance on fossil fuels. Therefore, currently, there is intensive research in this area. 1-4 Among the various energy sources available, sunlight provides a large amount of clean energy.⁵ In nature, solar energy is efficiently converted to chemical energy via photosynthesis.⁶ One potential approach to mimic this process in nonbiological solar energy systems, such as the "Artificial Leaf", has been investigated to capture solar energy and "split water" to generate hydrogen fuel." However, one major challenge in such artificial systems is the large overpotential caused by the high energy barrier of anodic oxygen evolution reaction (OER), a process that involves the transfer of four electrons per molecule of O₂ generated.^{3,8} To improve the efficiency of O₂ evolution (or water oxidation), significant efforts have been made to develop promising OER catalysts. Noble metal oxides, including IrO2 and RuO2, have been identified as highly efficient water oxidation catalysts. However, their high cost and toxicity make large-scale application infeasible. $^{9-11}$ As a result, attention has shifted to low-cost, abundant, and efficient metal-oxide catalysts, such as the first-row transition-metal-containing catalysts cobalt phosphate (CoPi) and NiFeO_x. 3,12,13 It is worth noting that to produce the majority of oxygen gas in the atmosphere, nature employs the highly efficient photosystem II as the biological catalyst, where the oxygen-evolving complex (OEC) $\rm Mn_4O_5Ca$ (Figure 1) is the active site for water oxidation. 14 The OEC complex consists of a cubane-like structure of $\rm Mn_3O_4Ca$ with an outer manganese atom connected by two μ -oxo ligands. 15 Although the oxygen evolution mechanism of the OEC in photosystem II remains elusive, the structural/

Received: December 16, 2023 Revised: April 13, 2024 Accepted: April 15, 2024 Published: April 24, 2024





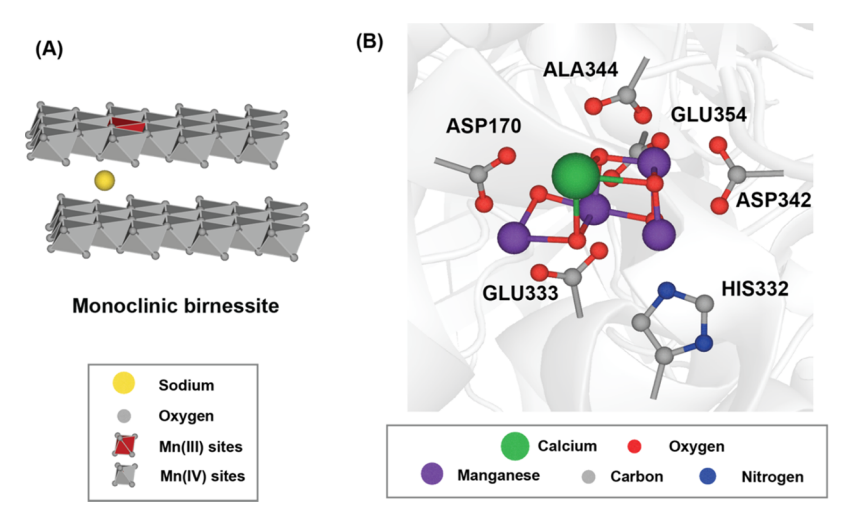


Figure 1. Crystal structure models of (A) monoclinic birnessite (cif: 9001270) and (B) the dark state of the oxygen evolution complex (OEC) in photosystem II (PDB: 5KAF). The OEC structure was reproduced with permission from ref 15. Copyright 2016 Springer Nature.

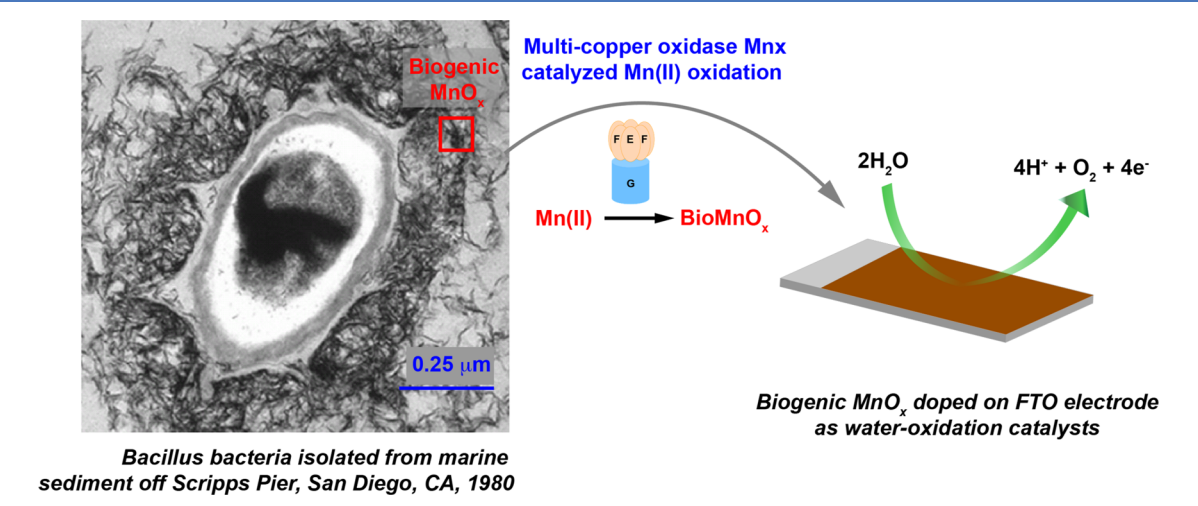


Figure 2. Overview of investigating the catalytic water oxidation potential of the biogenic MnO_x (Bio MnO_x). Tunneling electron micrograph (TEM) of a spore from *Bacillus* sp. SG-1 with biogenic MnO_x formed on the exosporium. The spore was isolated from marine sediment off Scripps pier, San Diego, CA, 1980. ^{60,61} The TEM image was adapted with permission from ref 61. Copyright 1999 Caister Academic Press.

elemental similarity between the OEC and manganese oxides has inspired a significant amount of research on exploring manganese-oxide catalysts. $^{16-20}$ For example, one of the commonly studied manganese-oxide OER catalysts is layered birnessite, which consists of an edge-sharing lattice of octahedral manganese-oxide units and intercalating alkaline metal cations between layers to balance the negative charges created by defects (Figure 1). $^{17,21-23}$

While most of the manganese oxides are synthesized using strong oxidants, ^{24–26} strong bases, ¹⁶ or external electric potentials to oxidize Mn(II), ^{22,27–29} manganese oxide minerals in nature are usually synthesized through enzymatic pathways under mild conditions. Abiotic oxidation of soluble Mn(II) to Mn(III) and Mn(IV) oxides usually proceeds slowly in seawater (pH 8.16). ^{30,31} However, manganese-oxidase enzymes can expedite this process by 3–5 orders of magnitude. ³² Within the marine *Bacillus* bacteria, a multicopper oxidase, MnxG, has been found to enzymatically generate manganese oxides via Mn(II) oxidation. ^{33,34} In 2013, MnxG was first expressed and purified in the form of a protein complex, named Mnx, where the MnxG (~138 kDa) subunit is combined with three MnxE (~12 kDa each) and three

MnxF (~12 kDa each) accessory protein subunits. 35,36 Since then, the Mn(II)-oxidation mechanism and the structure of Mnx have been intensively investigated via electron paramagnetic resonance (EPR) spectroscopy and kinetics studies. 34,37-39 In addition, the product of Mn(II)-oxidation catalyzed by Mnx has been characterized as defected and layered Mn(III,IV) oxides with a rod-shaped morphology. 40,41 However, the potential of biogenic manganese oxides as an OER catalyst has yet to be explored. Here, we employ the Mnx enzyme to synthesize biogenic manganese-oxide catalysts (denoted by biogenic MnO_x). We investigate the efficiency of biogenic MnOx as the catalyst for the OER under nearneutral pH conditions (Figure 2). By utilizing a combination of microscopic and spectroscopic techniques, including scanning electron microscopy (SEM), X-ray absorption spectroscopy (XAS), X-ray photoelectron spectroscopy (XPS), and electron paramagnetic resonance (EPR) spectroscopy, we have established the structure-function relationship between biogenic MnO_r and the OER activity. This work provides insights into the development of efficient OER catalysts that can be produced using a gentle and sustainable process.

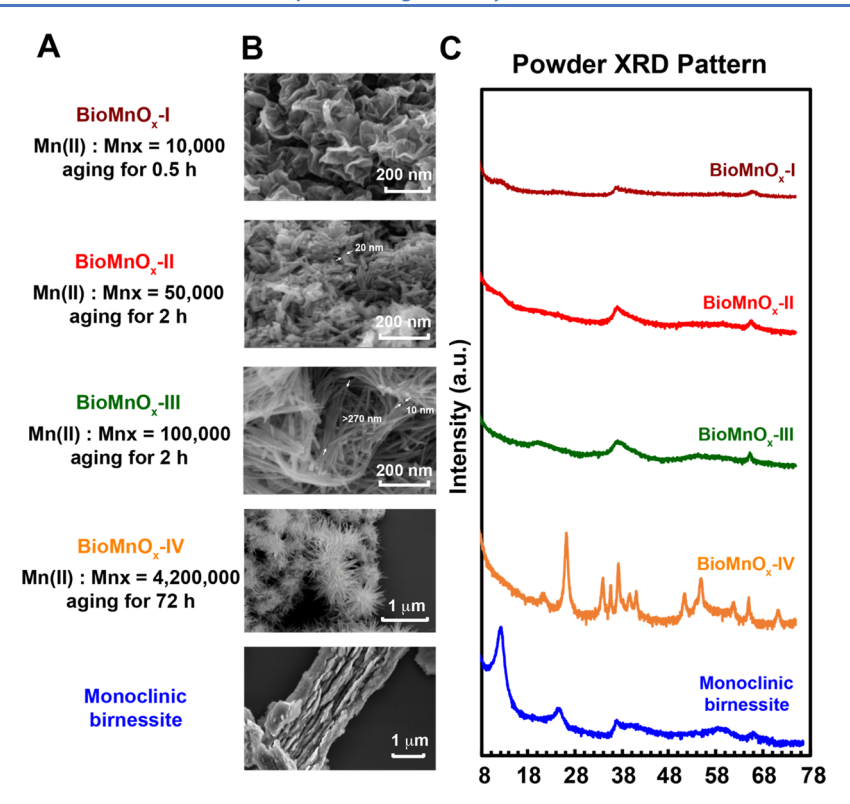


Figure 3. (A) Protocols for synthesizing $BioMnO_x$ samples. (B) Scanning electron micrographs (SEM) of $BioMnO_x$ -I, -II, -III, and IV, and monoclinic birnessite with the scale bars provided. The length and width of $BioMnO_x$ -II and -III are denoted. (C) pXRD spectra of $BioMnO_x$ samples and monoclinic birnessite.

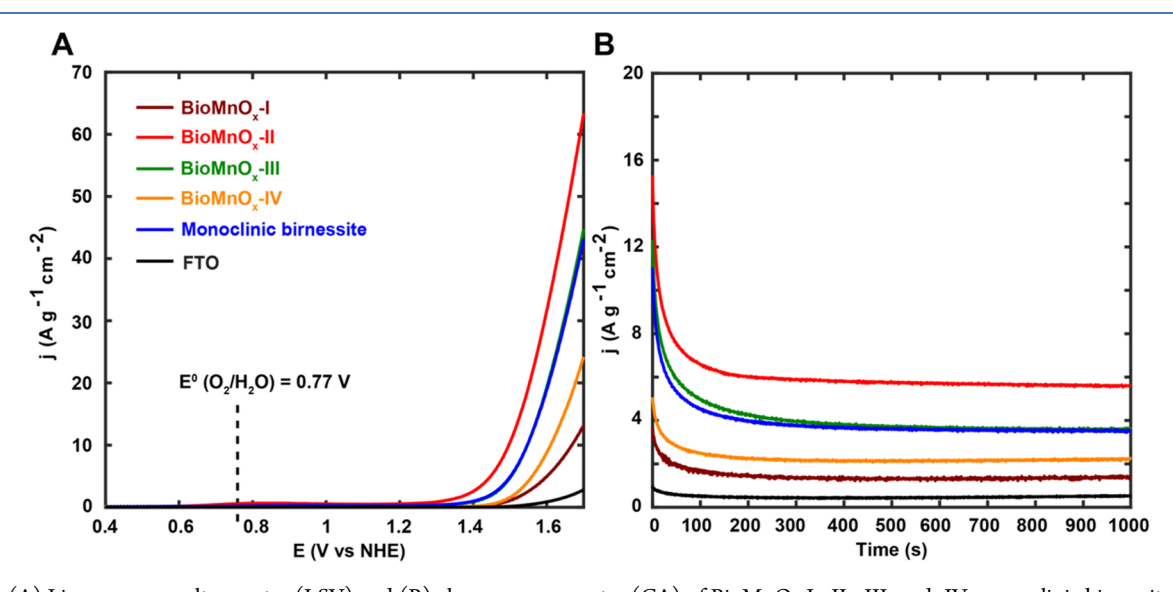


Figure 4. (A) Linear sweep voltammetry (LSV) and (B) chronoamperometry (CA) of BioMnO_x-I, -II, -III, and -IV, monoclinic birnessite, and bare FTO plate as a control (black). LSV was taken with a scan rate of 10 mV/s. CA was measured at 1.6 V (vs NHE, η = 830 mV). The current density was normalized to the weight of the catalysts (12 μ g). The electrolyte is 0.5 M NaPi (pH 7.8).

2. RESULTS AND DISCUSSION

2.1. Synthesis of Biogenic MnO_x with Diverse Morphologies and Crystalline Structures. As shown in Figure 3, the biogenic MnO_x samples with diverse morphologies and crystalline structures were synthesized by varying the ratio of Mn(II) to Mnx protein (denoted as Mn(II)/Mnx) and the mineralization time. When the ratio of Mn(II)/Mnx was as low as 10,000, and mineralization was allowed to continue for 0.5 h, the biogenic MnO_x showed a uniform "cabbage-like" morphology (BioMnO_x-I, Figure 3B).

Increasing the ratio of Mn(II)/Mnx to 50,000 and the length of mineralization to 2 h, the morphology of the biogenic MnO_x became sets of short-ordered "rods" with a length of \approx 100 nm and a diameter of \approx 20 nm (BioMnO_x-II, Figure 3B). When the ratio of Mn(II)/Mnx was increased to 100,000, long-ordered "rod-net" biogenic MnO_x formed, with the diameter of the rods \approx 10 nm (BioMnO_x-III, Figure 3B). Powder X-ray diffraction (pXRD) patterns (Figure 3C) of these three types of biogenic MnO_x show weak and broad peaks, indicating that the samples with a short mineralization time (\leq 2 h) are

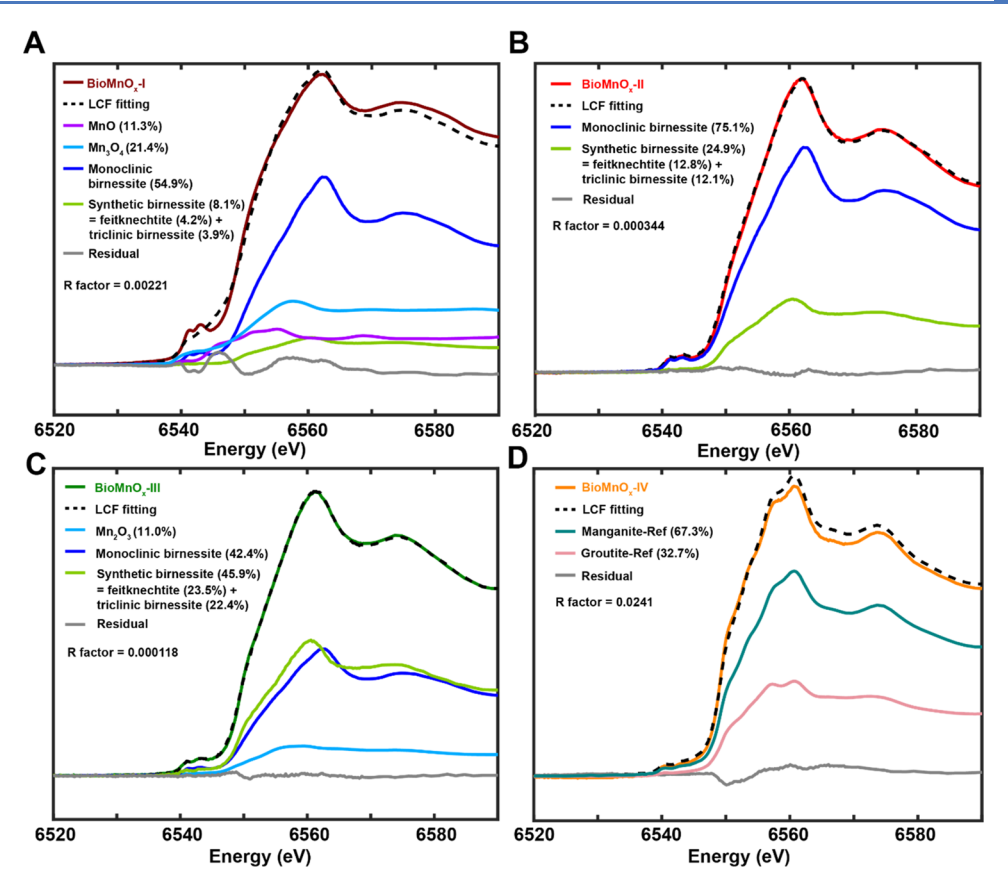


Figure 5. Mn K-edge XANES linear combination fitting (LCF) spectra of BioMnO_x-I (A), -II (B), -III (C), and -IV (D). The synthetic birnessite consisting of feitknechtite (51.3%) and triclinic birnessite (48.7%) is used as an LCF standard and the percentage of each component is provided (as shown in Figure S7). Manganite-Ref and Groutite-Ref are the Mn K-edge XANES spectra of manganite and groutite from the ref 47. The Manganite-Ref and Groutite-Ref data were adapted with permission from ref 47. Copyright 2012 Mineralogical Society of America.

amorphous and lack long-range ordering. Further increasing the ratio of Mn(II)/Mnx to as high as 4,200,000 and extending the mineralization time to as long as $\approx 72~\rm h$, the biogenic MnO $_x$ crystallized to form the "fiber-like" MnO $_x$ solids (BioMnO $_x$ -IV, Figure 3B). The pXRD pattern of BioMnO $_x$ -IV showing long-range ordered crystalline structures contains manganite (84.28%, Crystallography Open Database, COD, ID: 9009774) and groutite (15.72%, COD ID: 9011546), both of which are polymorphs of Mn^IIIO(OH) (see Figure S1). ⁴² In addition, as a standard control, monoclinic birnessite was synthesized via the electrodeposition method (see Methods for details), ⁴³ with its characteristic pXRD peaks at 12, 26, and 38° (Figure 3C).

Based on the different morphologies and crystalline structures of biogenic MnO_x , we propose the following mechanism for forming biogenic MnO_x . The initially generated MnO_x solids coat around the Mnx protein complex (Note: the diameter of the Mnx protein complex is ≈ 10 nm. 36) by forming the "cabbage-like" MnO_x morphology (Bio MnO_x -I). When more Mn(II) in the aqueous solution (corresponding to a higher ratio of Mn(II)/Mnx) is available, the cabbage-shaped MnO_x further grows along one direction by forming rods (Bio MnO_x -II) or rod-net structures (Bio MnO_x -III), or eventually crystallizing into the fiber-like manganite/groutite structures (Bio MnO_x -IV).

2.2. OER Activities of Biogenic MnO_x. Having synthesized the above sets of biogenic MnO_x with diverse morphologies and structures, we employed them as electrocatalysts for water-oxidation reactions as previous reports

suggested that synthetic MnO_x with varying morphologies show varying OER activities. ^{22,41,44,45} Both linear sweep voltammetric (LSV) and chronoamperometric (CA) studies were performed. As shown in Figure 4, all these biogenic MnO_x show activities for anodic O₂ evolution, i.e., employing smaller overpotentials (η < 880 mV at 8.3 A/g·cm², normal hydrogen electrode which is used through this paper) than that of the bare FTO electrode (η > 930 mV at 8.3 A/g·cm² vs NHE, Figure 4A) and showing higher CA current density at 1.6 V (vs NHE) (Figure 4B).

Especially, while the amorphous BioMnO_x-III exhibits comparable activity ($\eta \approx 760$ mV) for O₂ evolution to the standard monoclinic birnessite, the BioMnO_x-II shows a much higher activity for O₂ evolution, with η ca. 700 mV, i.e., 60 mV smaller than that of monoclinic birnessite. In addition, the CA current density of BioMnO_x-II at 1.6 V (vs NHE) was stabilized at ≈ 6 A/g·cm², which is 2 A/g·cm² higher than that of monoclinic birnessite (Figures 4B and S2 and S3). The BioMnO_x-II also exhibits a higher electrochemically active surface area (ECSA) than the monoclinic birnessite (see Figure S4 and Table S2).

2.3. Mn K-edge XANES of Biogenic MnO_x. We employed X-ray absorption spectroscopy (XAS) to investigate the bulk structural composition of biogenic MnO_x, due to the noncrystalline property of BioMnO_x-II and BioMnO_x-III. Linear combination fitting (LCF) analysis on the Mn K-edge XANES region (Figure S5) was performed by employing a set of standard manganese oxides (Figure S6), including monoclinic birnessite (COD ID: 9001270), synthetic

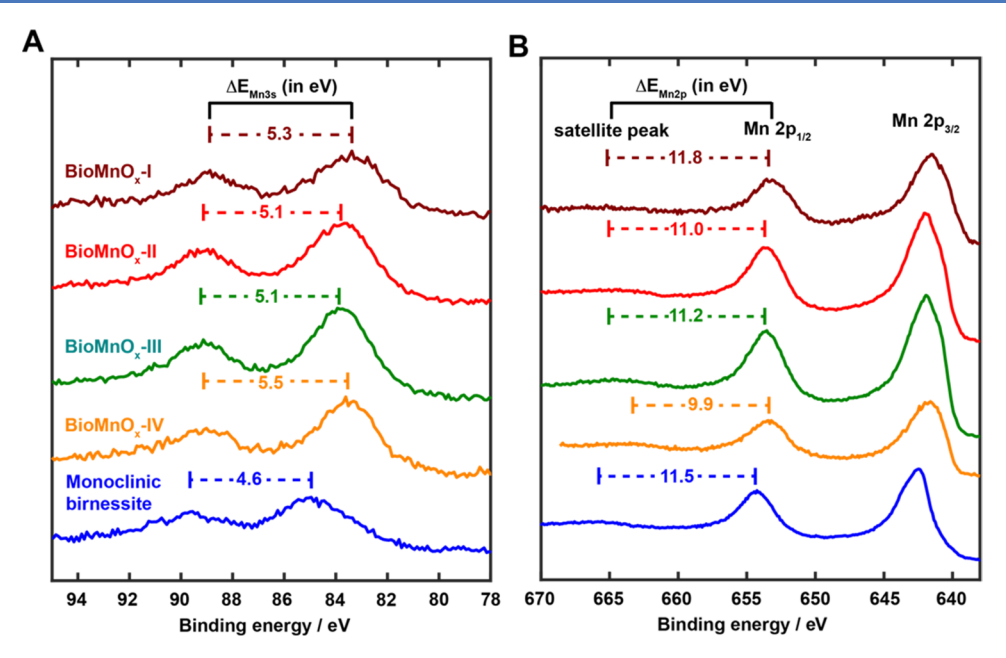


Figure 6. (A) Mn 3s XPS and (B) Mn 2p XPS of biogenic MnO_x samples and monoclinic birnessite.

birnessite (Figure S7), β -MnO₂ (COD ID: 1514117), Mn₂O₃ (COD ID: 1514103), Mn₃O₄ (COD ID: 1514104), and MnO (COD ID: 1010393). As shown in Figure 5, BioMnO_x-II consists of 75.1% monoclinic birnessite, as well as 12.8% feitknechtite⁴⁶ and 12.1% triclinic birnessite; meanwhile, BioMnO_x-III consists of 42.4% monoclinic birnessite, as well as 23.5% feitknechtite, 22.4% triclinic birnessite, and 11.0% Mn₂O₃. LCF analysis suggests that monoclinic birnessite is the major component for both BioMnO_x-III and BioMnO_x-III, which could be the reason that these two samples show at least comparable OER activity to monoclinic birnessite. To be noted that, for BioMnO_x-I, monoclinic birnessite is also the major component (54.9%, Figure 5). However, achieving a homogeneous suspension sample of BioMnO_x-I was challenging (different from the other samples), which could affect the attachment of the suspension onto the surface of the FTO electrode. Therefore, the low activity of BioMnO_x-I (Figure 4) that we measured may not correspond to its actual catalytic activity (vide infra). In the following sections, we will not correlate the surface properties of BioMnO_x-I with the measured activity and will focus on understanding the key to the activity of BioMnO_x-II and BioMnO_x-III. In addition, for $BioMnO_x$ -IV, consistent with pXRD analysis (vide supra), LCF analysis suggests that it contains manganite (67.3%) and groutite (32.7%),⁴⁷ both of which show lower activity than monoclinic birnessite (Figures 5 and S8 and S9). This explains the low level of the OER activity of BioMnO_x-IV, as shown in Figure 4.

2.4. Spectroscopic Characterization of Surface Mn Species. To understand the origin of the higher and comparable activity of $BioMnO_x$ -II and $BioMnO_x$ -III, as compared to the standard monoclinic birnessite, respectively, we employed XPS and EPR spectroscopy to characterize the surface Mn oxidation states of biogenic MnO_x .

Figure 6A,B shows Mn 3s and Mn 2p XPS spectra of the biogenic MnO_x catalysts, respectively. Three XPS spectroscopic features are related to the surface Mn oxidation state: (1) the energy splitting ($\Delta E_{\rm Mn~3s}$) in Mn 3s spectra: the lower $\Delta E_{\rm Mn~3s}$, the higher oxidation state of surface Mn;⁴⁸ (2) Mn

2p_{3/2} binding energy: high binding energy of Mn 2p suggests a high oxidation state of surface Mn species;⁴⁹ (3) the energy splitting $(\Delta E_{
m Mn~2p})$ between the Mn $2p_{1/2}$ and the satellite peak (the broad peak as indicated in Figure 6B): the lower $\Delta E_{\text{Mn 2p}}$, the lower oxidation state of surface Mn species.⁴⁸ Therefore, as summarized in Table 1, the oxidation state of Mn of BioMnO_x-IV is the lowest (see Table 1), as the XPS spectra show the lowest Mn 2p_{3/2} binding energy (641.8 eV), the smallest $\Delta E_{\text{Mn 2p}}$ (9.9 eV), and the largest $\Delta E_{\text{Mn 3s}}$ (5.5 eV). This is consistent with its crystalline structures containing manganite and groutite, both of which are polymorphs of Mn^{III}O(OH). In addition, the surface of BioMnO_x-II and BioMnO_x-III consists of a mixture of Mn(III) and Mn(IV) species, with $\Delta E_{
m Mn~3s}$ and $\Delta E_{
m Mn~2p}$ ca. 5.1 and 11.0 eV, respectively, while monoclinic birnessite contains more surface Mn(IV) by showing lower $\Delta E_{\text{Mn }3s}$ (4.6 eV) and larger $\Delta E_{\text{Mn }2p}$ (11.5 eV).

We further employed X-band parallel-mode continuouswave (CW) EPR spectroscopy to probe the surface Mn(III) species, as it has been considered as the key for OER activities in previous studies.⁵⁰ Five- or six-coordinate Mn(III) ions $(3d^4)$ are typically high-spin with a total spin of S = 2. For such an integer spin system of S = 2 (e.g., Mn(III)⁵¹⁻⁵³ and Fe(II)^{54,55}), transitions between the $M_s = 1 \pm 2$ > spin manifold can be detected by using parallel polarization $(B_0 \parallel B_1)$ or a high-field EPR technique. Here, for probing surface Mn(III), pyrophosphate (PP) was employed as the chelator of surface Mn(III) of the BioMnO_x samples. As shown in Figure 7, EPR spectra of BioMnO_x-I, BioMnO_x-II, and BioMnO_x-III show a sextet centered at ~80 mT ($g_{\text{eff}} = 8.20$) with ⁵⁵Mn (I = 5/2) hyperfine splitting of 140 MHz, which is a typical signal of Mn(III)PP. 38,56 The EPR signals suggest the presence of Mn(III) species at the surface of BioMnO_x-I, BioMnO_x-II, and BioMnO_x-III, which is consistent with the above XPS analysis. In contrast, no Mn(III)PP signal was detected for the crystallized samples of BioMnO_x-IV, monoclinic birnessite, and the Mn₂O₃ standard, implying the absence of Mn(III) species at the surface that are accessible and chelated by PP, as depicted in Figure 7.

Table 1. Summary of Mn 2p and 3s XPS Experimental Values of Manganese Oxides with Mn Oxidation States between II and IV

	Mn oxidation state	Mn 2p _{3/2} binding energy (eV)	ΔMn_{2p} splitting (eV)	ΔMn_{3s} splitting (eV)	references
MnO	II	640.7	6.3	5.9	Oku et al. ⁶²
	II	640.9		6.1	Foord et al. ⁶³
	II	641.7		5.5	Carver et al. ⁶⁴
	II	640.9		5.6	Nelson et al. ⁶⁵
	II		6.0	6.0	Gorlin et al. ⁶⁶
	II		6.0	6.0	Gorlin et al. ⁶⁷
	II			6.1	Ilton et al. ⁶⁸
	II			5.7	Namgung et al. ⁴²
	II			5.7	Cerrato et al. ⁶⁹
	2.0			6.2	Galakhov et al. ⁷⁰
	II			5.2	Lee et al. ⁷¹
	II	640.8		5.8	Junta and Hochella
	II			5.8	Murray et al. ⁷²
$\mathrm{Mn_3O_4}$	II, III	641.4	10.5	5.3	Oku et al. ⁶²
	II,III	641.0		5.6	Nelson et al. ⁶⁵
	II, III		10.5	6.0	Gorlin et al. ⁶⁶
	II, III		10.3	5.8	Gorlin et al. ⁶⁷
	II, III			5.6	Murray et al. ⁷²
	II,III			5.2	Lee et al. ⁷¹
	2.66			5.6	Galakhov et al. ⁷⁰
	2.68-2.85	641.5		5.45	Han et al. ⁷³
Mn_2O_3	III (α)	641.9	10.0	5.2	Oku et al. ⁶²
	III (γ)	641.7		5.2	Oku et al. ⁶²
	III	641.8		5.5	Foord et al. ⁶³
	III	641.8		5.4	Carver et al. ⁶⁴
	III	641.2		5.4	Nelson et al. ⁶⁵
	III		10.0	5.1	Gorlin et al. ⁶⁶
	III		10.0	5.1	Gorlin et al. ⁶⁷
	III			5.5	Namgung et al. ⁴²
	III			5.2-5.3	Cerrato et al. ⁶⁹
MnOOH	III (γ)	641.7		4.6	Oku et al. ⁶²
	III	01117		5.4	Ilton et al. ⁶⁸
	III (γ)			5.3	Murray et al. ⁷²
	III (γ)	641.7		5.4	Junta and Hochella
Mn_5O_8	II, IV	011.7		4.9	Murray et al. ⁷²
	II, IV			4.6	Lee et al. ⁷¹
MnO_2	$3.89 (\alpha)$			4.5	Sun et al. ⁷⁴
	$3.66 (\beta)$			4.7	Sun et al. ⁷⁴
	3.78 (γ)			4.6	Sun et al. ⁷⁴
	IV (β)	642.2	11.2	4.7	Oku et al. ⁶²
	IV (p) IV	642.5	11.2	4.5	Foord et al. ⁶³
	IV	642.4		7.5	Carver et al. ⁶⁴
	IV IV	641.9		4.5	Nelson et al. ⁶⁵
	IV IV	041.9	11.8		Gorlin et al. 66
				4.5	Gorlin et al. 67
	IV		11.8	4.5	
	IV		11.8	4.5	Pinaud et al. ⁴³
	IV			4.4	Ilton et al. ⁶⁸
	IV (β)			4.9	Namgung et al. ⁴²
	IV			4.6	Murray et al. ⁷²
	IV	642.0		4.5	Junta and Hochella
	IV			4.5	Cerrato et al. ⁶⁹
Li ₂ MnO ₃	4.0			4.5	Galakhov et al. ⁷⁰
Na _{0.31} MnO _{1.9} nanofiber	3.32	642.4		5.1	Li et al. ⁷⁵
$La_{1-x}Sr_xMnO_3$	3.0-3.3			~5.3	Galakhov et al. ⁷⁰
Mn(III,IV) oxides	III, IV			5.0-5.1	Cerrato et al. ⁶⁹
BioMnO _x -I	II–IV	642.8	11.8	5.3	this work
BioMnO _x -II	III, IV	642.0	11.0	5.1	this work
BioMnO _x -III	III, IV	642.0	11.2	5.3	this work
BioMnO _x -IV monoclinic birnessite	III	641.9	9.9	5.5	this work

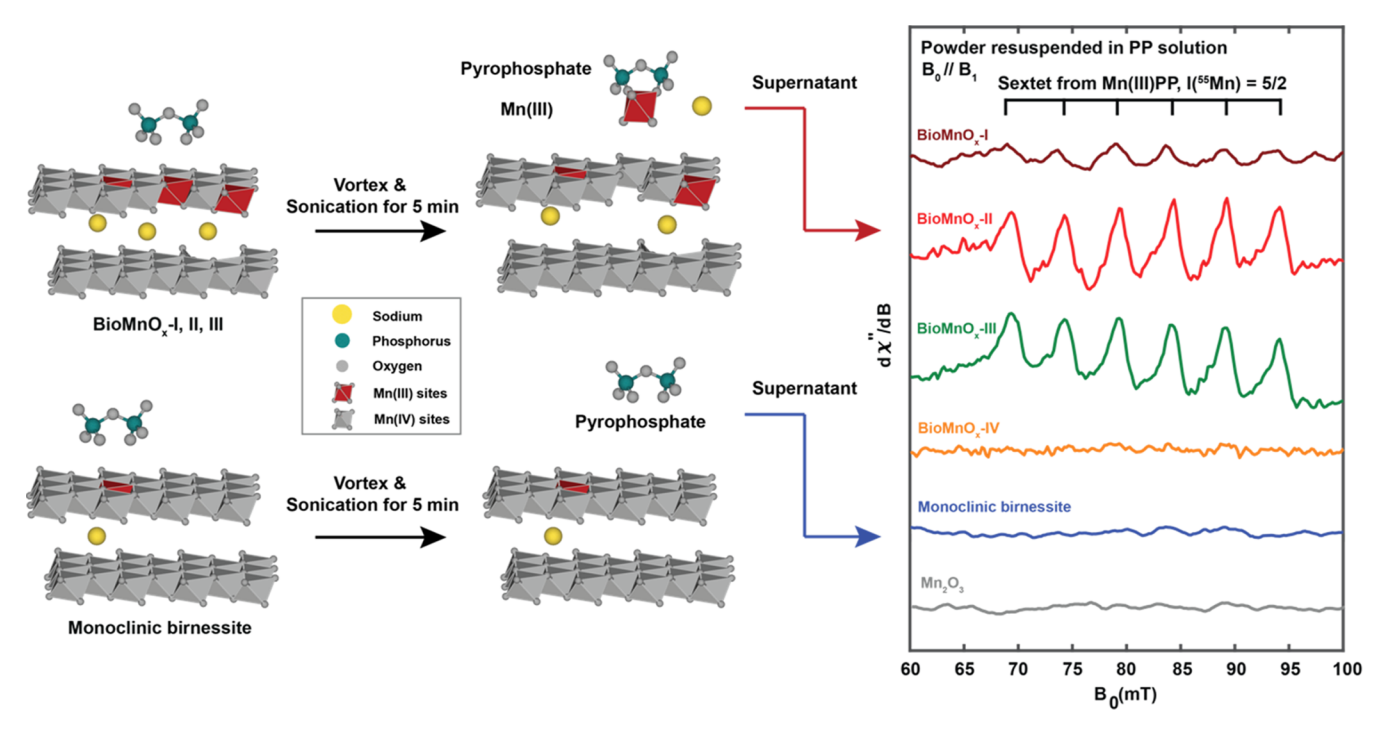


Figure 7. Depiction of the surface Mn(III) extraction by pyrophosphate (PP) on $BioMnO_x$ and monoclinic birnessite. The Mn(III)PP signals are shown on the X-band (9.37 GHz) parallel-mode EPR spectra. As a control experiment, the EPR spectrum of the standard Mn(III) oxide (Mn_2O_3) was measured and shown in the gray trace. The corresponding perpendicular-mode EPR spectrum of the powder $BioMnO_x$ -II is shown in Figure S10. The higher sodium content as an intercalating cation in the $BioMnO_x$ -II is supported by the energy-dispersive X-ray spectroscopy (Figure S11). EPR experimental parameters: temperature = 8 K; microwave frequency = 9.371 GHz; microwave power = 10 mW; conversion time = 40 ms; modulation amplitude = 0.8 mT; modulation frequency = 100 kHz.

Both XPS and EPR analyses suggest that the surface Mn(III) species contributes to the higher and comparable OER activity of $BioMnO_x$ -II and $BioMnO_x$ -III, as compared to the standard monoclinic birnessite, respectively.

3. CONCLUSIONS

In this work, we show that efficient OER manganese-oxide catalysts can be synthesized through a mild and tunable biological method. High OER activity of the biogenic MnO_x is achieved as compared to synthetic birnessite. Spectroscopic analysis suggests that the monoclinic-birnessite component, along with the surface Mn(III) species, is potentially crucial for the OER activity of biogenic MnO_x . This work provides valuable insights into the development of efficient OER catalysts that can be produced by using a gentle and sustainable process. Further investigations will focus on developing more efficient OER catalysts, for example, via the introduction of a second transition metal ion onto the surface of biogenic MnO_x .

4. METHODS

4.1. General Procedures and Materials. Milli-Q water (18 $M\Omega$ ·cm resistivity) was used to make solutions and rinse the electrodes and glassware. For the sample preparation, $MnSO_4$ · H_2O (MW 169.01 g/mol) was used as the $Mn^{2+}(aq)$ source. Mn_2O_3 powder (MW = 157.87 g/mol) was used as a reference Mn(III) oxide. Sodium pyrophosphate (NaPP, MW 265.90 g/mol) was used as the Mn(III) chelator. All chemicals were purchased from Sigma-Aldrich unless otherwise noted. All standard manganese oxides were also purchased from Sigma-Aldrich.

4.2. Overexpression and Purification of the Mnx **Protein Complex.** The Mnx protein complex (MnxE₃F₃G, \sim 211 kDa, denoted as Mnx) was overexpressed in Escherichia coli BL21(DE3) using the pASK/IBA3plus vector (IBA Lifesciences, Germany) containing the mnxEFG gene construct and Strep-tag II.³⁷ The protein was purified via Strep-tag affinity chromatography (IBA Lifesciences, Germany) and size exclusion chromatography with a HiLoad16/600 Superdex 200 pg (GE Healthcare, IL) column as described previously.³⁷ The eluted protein was dialyzed to remove excess Cu2+ and then was stored in the storage buffer containing 20 mM HEPES, 20 mM KCl, and 20% v/v ethylene glycol. The protein was quantified by a Thermo Scientific Pierce bicinchoninic acid (BCA) protein assay or by the extinction coefficient of T1Cu $(\varepsilon_{590 \text{ nm}} = 5600 \text{ M}^{-1} \cdot \text{cm}^{-1})$ in the Mnx protein complex. The final protein sample was flash frozen in liquid nitrogen and stored at -80 °C for following experiments.

4.3. Biogenic MnO_x (BioMnOx-I, -II, -III, or -IV) Sample Preparation. Biogenic MnO_x was synthesized via aerobic oxidation of Mn²⁺(aq) by the Mnx protein complex. As shown in Table S1, 10 μ L of 100 μ M Mnx protein was added to 50 mL of buffer solution (10 mM HEPES, 50 mM NaCl, pH = 7.8) in a conical polypropylene centrifuge tube under ambient conditions, with a final concentration of Mnx enzyme 20 nM. Then, a varying amount of MnSO₄ solution was added, and the tube was gently inverted 6–8 times to ensure thorough mixing (Table S1). The reaction mixture was incubated for varying lengths of time with the tube loosely capped to ensure sufficient oxygen supply. After incubation, the reaction mixture was centrifuged at 12,000 rpm for 30 min. The resulting biogenic MnO_x solid was then collected and washed five times with Milli-Q water, followed by gentle centrifugation (6000

rpm for 2 min). After washing, the biogenic MnO_x solid was air-dried at room temperature for 3 days. The resulting biogenic MnO_x was denoted as BioMnOx-I, -II, -III, or -IV (Table S1) based on the initial amount of $MnSO_4$ and the allowed mineralization time.

- 4.4. Synthesis of Synthetic Birnessite. Synthetic birnessite was synthesized using a protocol that was modified from a previously reported procedure. 57 First, MnCl₂·4H₂O solution (MW 197.91 g/mol, 3.166 g in 32 mL of H_2O) was added dropwise to NaOH solution (MW 40 g/mol, 11 g in 36 mL of H₂O), followed by vigorously stirring to generate Mn(OH)₂ (pink precipitates). Then, KMnO₄ solution (MW 158.034 g/mol, 1 g in 32 mL of H₂O) was added dropwise to the above mixture to yield dark gray precipitates. After being stirred for 1 h, the mixture was heated at 55 °C for 24 h. Then, the supernatant was discarded, and the remaining suspension was centrifuged at 27,500g for 20 min. The resulting solid was collected, washed 5 times using 1 M NaCl, and then washed 10 times with Milli-Q water to remove excessive salts and bases. Finally, the synthetic birnessite powder was collected by lyophilization and characterized by powder X-ray diffraction (pXRD). This synthetic birnessite sample was also used as one of the X-ray absorption near-edge structure (XANES) spectroscopy standards for Mn K-edge XANES linear combination fitting (LCF) analysis.
- 4.5. Synthesis of Monoclinic Birnessite. The monoclinic birnessite sample was prepared using a protocol that was modified from previously reported procedures. 22,43 Electrodeposition was performed on a Princeton Applied Research (Oak Ridge, TN) Model 263 A potentiostat/galvanostat and was analyzed using the PowerStep software package in a threeelectrode system. The three-electrode system contains a fluorine-doped tin oxide-coated glass (FTO; Sigma-Aldrich, MO) as the working electrode, a nickel foam (MTI Corp., CA) as the counter electrode, and Ag/AgCl in 3 M NaCl (0.203 V vs NHE; BASi, IN) as the reference electrode. The birnessite sample was electrodeposited onto a FTO plate (10 cm × 9 cm) submerged in the electrolyte (2 mM MnSO₄ and 50 mM NaCl). During electrodeposition, a potential of 1.0 V (vs NHE) was applied for 300 s, followed by applying a potential of 1.2 V (vs NHE) until a total charge of ~27 C (~300 mC/ cm²) passed. The electrodeposited FTO plate was then washed three times with Milli-Q water and air-dried for 3 days. The monoclinic birnessite powder was obtained by gently scraping the film with a clean razor.
- 4.6. Electrochemical Measurements. Linear sweep voltammetry (LSV) and chromatoamperometry (CA) were conducted on a Princeton Applied Research Model 263 A potentiostat/galvanostat in a three-electrode system. The reference and counter electrodes were Ag/AgCl (3 M NaCl) and nickel foam, respectively. The working electrode was prepared by drop-casting 12 μ g of manganese-oxide sample from a sonicated suspension in Milli-Q water onto an area of 1 cm² of FTO plate and air-dried overnight. The LSV was measured from 0 to 1.5 V (vs Ag/AgCl), and the CA was taken at an overpotential of 830 mV for 1000 s. All LSV and CA measurements were conducted under stirring conditions in 0.5 M sodium phosphate buffer (pH 7.8). For all electrochemical measurements, the first LSV and CV curves were measured to charge the double layer and to remove the air-oxidized surface layer. Then, the second LSV and CA curves were recorded and taken as the electrochemical data in this work.

- **4.7. Electrochemically Active Surface Area (ECSA).** The ECSA was calculated from the measurements of cyclic voltammetry at different scan rates. The potential ranging from 350 to 515 mV was chosen to minimize the faradaic current response. The CV experiment was conducted in the stirring solution with the scan rates of 300, 200, 100, 50, 20, and 10 mV/s. The potential applied on the working electrode was held for 10 s to allow double-layer charging. The slope of the resulting "current vs scan rate" plot corresponds to the double-layer capacitance, $C_{\rm DL}$, which is equal to the ECSA multiplied by specific capacitance, $C_{\rm S}$: slope = $C_{\rm DL}$ = (ECSA) \times $C_{\rm S}$.
- **4.8. Powder X-ray Diffraction (pXRD).** pXRD patterns were measured on a Bruker D8 ADVANCE Eco instrument by using Cu K α irradiation (λ = 0.154 nm). The sample was grounded and filtered through a 100-mesh sieve to obtain fine powder, which was then mounted onto the SiO₂ zero-background plate via an ethanol solvent smear. pXRD measurement was performed with 2 θ ranging from 5° to 75° in 3421 steps. The pattern was background-corrected, K $_{\alpha 2}$ -stripped, and peak-matched using the Crystallographic Open Database (COD).
- **4.9. Scanning Electron Microscopy (SEM).** SEM was performed with a Thermo Fisher Quattro S at Advanced Materials Characterization and Testing Laboratory (AMCaT) at the University of California, Davis. SEM samples were prepared by drying a droplet of the sample suspension on a silicon wafer. The surface morphology of the sample was examined by using an Everhart-Thornley detector (ETD) with an acceleration voltage of 5 kV and a spot size of 2.5 Å.
- **4.10.** X-ray Photoelectron Spectroscopy (XPS). High-resolution XPS of manganese was obtained with an Al $K\alpha$ source (PHI 5000 VersaProbe, Physical Electronics, Enzo, Chigasaki, Japan). All measurements were performed on the carbon tape and calibrated to the adventitious carbon 1s peak at 284.8 eV.
- 4.11. Electron Paramagnetic Resonance (EPR) Spectroscopy. Manganese oxide powder was grounded and filtered through a 100-mesh sieve. Fine manganese-oxide powder (\sim 0.3 mg) was suspended in 200 μ L of sodium pyrophosphate solution (20 mM NaPP and 20% ethylene glycol) via vortex mixing and sonication. The mixture was centrifuged at 13,300 rpm (\sim 20,000 g) for 30 s. The supernatant was then pipetted into an X-band EPR tube and frozen in liquid nitrogen. X-band continuous-wave (CW) EPR spectra were recorded by using an EleXsys E500 spectrometer (Bruker, Billerica, MA). Cryogenic temperatures were achieved and controlled using an ESR900 liquid helium cryostat in conjunction with a temperature controller (Oxford Instruments ITC503) and a gas flow controller. Parallel-mode EPR experiments $(B_0 \parallel B_1)$ were performed with a dual-mode resonator (ER4116DM). All CW EPR data were collected under slow-passage, nonsaturating conditions. Spectrometer settings were as follows: conversion time = 40 ms, modulation amplitude = 0.8 mT, and modulation frequency = 100 kHz; other settings are given in the corresponding figure captions.
- 4.12. X-ray Absorption Spectroscopy (XAS) and Data Analysis. All XAS scans were taken at the Stanford Synchrotron Radiation Lightsource (SSRL) and at the SLAC National Accelerator Laboratory. Powder samples were taken in either beamline stations 4–3 or 2–2. Energy calibration of the beam was performed using elemental Mn for the Mn Kedge. The fluorescence data were collected using a Lytle

ACS Catalysis pubs.acs.org/acscatalysis Research Article

detector or Ge detector and then averaged together to increase the signal-to-noise ratio.

X-ray absorption near-edge structure (XANES) data were analyzed by using the Athena package within the Demeter XAS-processing software. Scans of each sample were aligned and averaged to generate a merged spectrum. All the Mn Kedge XAS spectra were calibrated by setting the third peak of the Mn foil spectrum in the reference channel to the edge energy of Mn, i.e., 6539 eV. The average oxidation states of Mn in manganese-oxide samples were estimated using the method described by Wong et al. 59 The Mn K-edge XANES spectra of MnO, Mn₃O₄, Mn₂O₃, β -MnO₂, and synthetic birnessite were collected and used as standard components for linear combination fitting (LCF). All fitting components were forced to be positive contributions, but the percentage sum was not forced to 1 to allow the presence of unknown compositions. The R-factor, $\frac{\sum (\text{data} - \text{fit})^2}{\sum \dots^2}$, was reported as a reference for the fitting quality.

ASSOCIATED CONTENT

Data Availability Statement

All data are available in the manuscript or the Supporting Information.

Solution Supporting Information

The Supporting Information is available free of charge at https://pubs.acs.org/doi/10.1021/acscatal.3c06119.

Scheme of manganese oxide sample preparation; electrochemical activity and stability; composition analysis of $BioMnO_x$ and other manganese oxide standards; details of powder X-ray diffraction (pXRD); linear sweep voltammetry (LSV) and chronoamperometry (CA) of control samples; perpendicular-mode X-band continuous-wave EPR; energy-dispersive X-ray (EDS) spectra (PDF)

AUTHOR INFORMATION

Corresponding Authors

Lizhi Tao — Department of Chemistry, University of California, Davis, California 95616, United States; Present Address: Department of Chemistry, Southern University of Science and Technology, Shenzhen 518055, China; orcid.org/0000-0001-9921-2297; Email: taolz@sustech.edu.cn

R. David Britt — Department of Chemistry, University of California, Davis, California 95616, United States;
orcid.org/0000-0003-0889-8436; Email: rdbritt@ucdavis.edu

Authors

Wen Fu — Department of Chemistry, University of California, Davis, California 95616, United States; ⊙ orcid.org/0000-0003-0744-4707

Forrest P. Hyler – Department of Chemistry, University of California, Davis, California 95616, United States

Joel Sanchez – Department of Chemical Engineering, Stanford University, Stanford, California 94035, United States

Thomas F. Jaramillo — Department of Chemical Engineering, Stanford University, Stanford, California 94035, United States; © orcid.org/0000-0001-9900-0622 Jesús M. Velázquez – Department of Chemistry, University of California, Davis, California 95616, United States;

orcid.org/0000-0003-2790-0976

Complete contact information is available at: https://pubs.acs.org/10.1021/acscatal.3c06119

Notes

The authors declare no competing financial interest.

ACKNOWLEDGMENTS

We thank Prof. William Casey (University of California, Davis), Prof. Thomas Spiro, and Prof. Bradley Tebo (University of Washington, Seattle) for helpful discussions. This work was supported by the National Science Foundation award number CHE-1665455 to R.D.B. The use of the Stanford Synchrotron Radiation Lightsource, SLAC National Accelerator Laboratory, is supported by the U.S. Department of Energy, Office of Science, Office of Basic Energy Sciences under Contract No. DE-AC02-76SF00515. The XPS measurements and analysis were supported by the U.S. Department of Energy, Office of Science, Office of Basic Energy Sciences, Chemical Sciences, Geosciences, and Biosciences Division, Catalysis Science Program to the SUNCAT Center for Interface Science and Catalysis. J.M.V. thanks the University of California, Davis, for start-up funding, as well as support from the Cottrell Scholar program supported by the Research Corporation for Science Advancement (RCSA 26780). J.M.V. acknowledges funding support from the NSF through the Faculty Early Career Development Program (DMR-2044403).

REFERENCES

- (1) Gray, H. B. Powering the Planet with Solar Fuel. *Nat. Chem.* **2009**, *1* (1), 7 DOI: 10.1038/nchem.141.
- (2) Cook, T. R.; Dogutan, D. K.; Reece, S. Y.; Surendranath, Y.; Teets, T. S.; Nocera, D. G. Solar Energy Supply and Storage for the Legacy and Nonlegacy Worlds. *Chem. Rev.* **2010**, *110* (11), 6474–6502.
- (3) Song, F.; Bai, L.; Moysiadou, A.; Lee, S.; Hu, C.; Liardet, L.; Hu, X. Transition Metal Oxides as Electrocatalysts for the Oxygen Evolution Reaction in Alkaline Solutions: An Application-Inspired Renaissance. J. Am. Chem. Soc. 2018, 140 (25), 7748–7759.
- (4) Chu, S.; Majumdar, A. Opportunities and Challenges for a Sustainable Energy Future. *Nature* **2012**, 488 (7411), 294–303.
- (5) Lewis, N. S.; Nocera, D. G. Powering the Planet: Chemical Challenges in Solar Energy Utilization. *Proc. Natl. Acad. Sci. U. S. A.* **2006**, 103 (43), 15729–15735.
- (6) Calvin, M. The Path of Carbon in Photosynthesis. J. Chem. Educ. 1949, 26 (12), 639.
- (7) Nocera, D. G. The Artificial Leaf. Acc. Chem. Res. 2012, 45 (5), 767-776.
- (8) Suen, N.-T.; Hung, S.-F.; Quan, Q.; Zhang, N.; Xu, Y.-J.; Chen, H. M. Electrocatalysis for the Oxygen Evolution Reaction: Recent Development and Future Perspectives. *Chem. Soc. Rev.* **2017**, *46* (2), 337–365.
- (9) Hunter, B. M.; Gray, H. B.; Mu, A. M.; Müller, A. M. Earth-Abundant Heterogeneous Water Oxidation Catalysts. *Chem. Rev.* **2016**, *116* (22), 14120–14136.
- (10) Morris, N. D.; Suzuki, M.; Mallouk, T. E. Kinetics of Electron Transfer and Oxygen Evolution in the Reaction of [Ru(Bpy)₃]³⁺ with Colloidal Iridium Oxide. *J. Phys. Chem. A* **2004**, *108* (42), 9115–9119.
- (11) Nakagawa, T.; Beasley, C. A.; Murray, R. W. Efficient Electro-Oxidation of Water near Its Reversible Potential by a Mesoporous IrOx Nanoparticle Film. *J. Phys. Chem. C* **2009**, *113* (30), 12958–12961.

- (12) Mccrory, C. C. L.; Jung, S.; Ferrer, I. M.; Chatman, S. M.; Peters, J. C.; Jaramillo, T. F. Benchmarking Hydrogen Evolving Reaction and Oxygen Evolving Reaction Electrocatalysts for Solar Water Splitting Devices. *J. Am. Chem. Soc.* **2015**, *137*, 4347–4357, DOI: 10.1021/ja510442p.
- (13) Kanan, M. W.; Nocera, D. G. In Situ Formation of an Oxygen-Evolving Catalyst in Neutral Water Containing Phosphate and Co²⁺. Science 2008, 321 (5892), 1072–1075.
- (14) Bushneil, M. L. Architecture of the Environment. Des. Autom. 1988, 303 (March), 101–117.
- (15) Young, I. D.; Ibrahim, M.; Chatterjee, R.; Gul, S.; Fuller, F. D.; Koroidov, S.; Brewster, A. S.; Tran, R.; Alonso-Mori, R.; Kroll, T.; Michels-Clark, T.; Laksmono, H.; Sierra, R. G.; Stan, C. A.; Hussein, R.; Zhang, M.; Douthit, L.; Kubin, M.; de Lichtenberg, C.; Vo Pham, L.; Nilsson, H.; Cheah, M. H.; Shevela, D.; Saracini, C.; Bean, M. A.; Seuffert, I.; Sokaras, D.; Weng, T.-C.; Pastor, E.; Weninger, C.; Fransson, T.; Lassalle, L.; Bräuer, P.; Aller, P.; Docker, P. T.; Andi, B.; Orville, A. M.; Glownia, J. M.; Nelson, S.; Sikorski, M.; Zhu, D.; Hunter, M. S.; Lane, T. J.; Aquila, A.; Koglin, J. E.; Robinson, J.; Liang, M.; Boutet, S.; Lyubimov, A. Y.; Uervirojnangkoorn, M.; Moriarty, N. W.; Liebschner, D.; Afonine, P. V.; Waterman, D. G.; Evans, G.; Wernet, P.; Dobbek, H.; Weis, W. I.; Brunger, A. T.; Zwart, P. H.; Adams, P. D.; Zouni, A.; Messinger, J.; Bergmann, U.; Sauter, N. K.; Kern, J.; Yachandra, V. K.; Yano, J. Structure of Photosystem II and Substrate Binding at Room Temperature. Nature 2016, 540 (7633), 453–457.
- (16) Pokhrel, R.; Goetz, M. K.; Shaner, S. E.; Wu, X.; Stahl, S. S. The "Best Catalyst" for Water Oxidation Depends on the Oxidation Method Employed: A Case Study of Manganese Oxides. *J. Am. Chem. Soc.* **2015**, *137* (26), 8384–8387.
- (17) Zaharieva, I.; Najafpour, M. M.; Wiechen, M.; Haumann, M.; Kurz, P.; Dau, H. Synthetic Manganese-Calcium Oxides Mimic the Water-Oxidizing Complex of Photosynthesis Functionally and Structurally. *Energy Environ. Sci.* **2011**, 4 (7), 2400–2408.
- (18) Najafpour, M. M.; Ehrenberg, T.; Wiechen, M.; Kurz, P. Calcium Manganese(III) Oxides (CaMn₂O₄:x H₂O) as Biomimetic Oxygen-Evolving Catalysts. *Angew. Chem., Int. Ed.* **2010**, 49 (12), 2233–2237.
- (19) Wiechen, M.; Najafpour, M. M.; Allakhverdiev, S. I.; Spiccia, L. Water Oxidation Catalysis by Manganese Oxides: Learning from Evolution. *Energy Environ. Sci.* **2014**, *7* (7), 2203.
- (20) Baricuatro, J. H.; Saadi, F. H.; Carim, A. I.; Velazquez, J. M.; Kim, Y.; Soriaga, M. P. Influence of Redox-Inactive Cations on the Structure and Electrochemical Reactivity of Synthetic Birnessite, a Heterogeneous Analog for the Oxygen-Evolving Complex. *J. Phys. Chem. C* 2016, 120, 15618–15631, DOI: 10.1021/acs.jpcc.5b07028.
- (21) Wiechen, M.; Zaharieva, I.; Kurz, P.; Dau, H.; Kurz, P. Layered Manganese Oxides for Water-Oxidation: Alkaline Earth Cations Influence Catalytic Activity in a Photosystem II-like Fashion. *Chem. Sci.* **2012**, *3* (7), 2330–2339.
- (22) Tao, L.; Stich, T. A.; Jaccard, H.; Britt, R. D.; Casey, W. H.; States, U. Manganese-Oxide Solids as Water-Oxidation Electrocatalysts: The Effect of Intercalating Cations. In *Advances in the Environmental Biogeochemistry of Manganese*; American Chemical Society, 2015.
- (23) Mckendry, I. G.; Thenuwara, A. C.; Shumlas, S. L.; Peng, H.; Aulin, Y. V.; Chinnam, P. R.; Borguet, E.; Strongin, D. R.; Zdilla, M. J. Systematic Doping of Cobalt into Layered Manganese Oxide Sheets. *Inorg. Chem.* **2018**, *57*, 557–564, DOI: 10.1021/acs.inorg-chem.7b01592.
- (24) McKenzie, R. M. The Synthesis of Birnessite, Cryptomelane, and Some Other Oxides and Hydroxides of Manganese *Mineral. Mag.*, **1971**, 38, 493–502 DOI: 10.1180/minmag.1971.038.296.12.
- (25) Najafpour, M. M.; Moghaddam, A. N. Nano-Sized Manganese Oxide: A Proposed Catalyst for Water Oxidation in the Reaction of Some Manganese Complexes and Cerium(IV) Ammonium Nitrate. *Dalton Trans.* **2012**, *41* (34), 10292.

- (26) Parent, A. R.; Crabtree, R. H.; Brudvig, G. W. Comparison of Primary Oxidants for Water-Oxidation Catalysis. *Chem. Soc. Rev.* **2013**, 42 (6), 2247–2252.
- (27) Ram, A.; Hillebrand, P.; Stellmach, D.; May, M. M.; Bogdano, P.; Fiechter, S. Evaluation of MnOx, Mn₂O₃, and Mn₃O₄ Electrodeposited Films for the Oxygen Evolution Reaction of Water. *J. Phys. Chem. C* **2014**, *118*, 14073–14081, DOI: 10.1021/jp500939d.
- (28) Kölbach, M.; Fiechter, S.; van de Krol, R.; Bogdano, P. Evaluation of Electrodeposited α -Mn₂O₃ as a Catalyst for the Oxygen Evolution Reaction. *Catal. Today* **2017**, 290, 2–9, DOI: 10.1016/j.cattod.2017.03.030.
- (29) Huynh, M.; Shi, C.; Billinge, S. J. L. L.; Nocera, D. G. Nature of Activated Manganese Oxide for Oxygen Evolution. *J. Am. Chem. Soc.* **2015**, 137 (47), 14887–14904.
- (30) Morgan, J. J. Kinetics of Reaction between O₂ and Mn (II) Species in Aqueous Solutions. *Geochim. Cosmochim. Acta* **2005**, 69 (1), 35–48.
- (31) Bargar, J. R.; Tebo, B. M.; Bergmann, U.; Webb, S. M.; Glatzel, P.; Chiu, V. Q.; Villalobos, M. Biotic and Abiotic Products of Mn(II) Oxidation by Spores of the Marine *Bacillus Sp.* Strain SG-1. *Am. Mineral.* **2005**, *90* (1), 143–154.
- (32) Spiro, T. G.; Bargar, J. R.; Sposito, G.; Tebo, B. M. Bacteriogenic Manganese Oxides. *Acc. Chem. Res.* **2010**, *43* (1), 2–9. (33) Dick, G. J.; Torpey, J. W.; Beveridge, T. J.; Tebo, B. M.; Al, D. E. T. Direct Identification of a Bacterial Manganese(II) Oxidase, the Multicopper Oxidase MnxG, from Spores of Several Different Marine Bacillus Species. *Appl. Environ. Microbiol.* **2008**, *74* (5), 1527–1534.
- (34) Tao, L.; Stich, T. A.; Butterfield, C. N.; Romano, C. A.; Spiro, T. G.; Tebo, B. M.; Casey, W. H.; Britt, R. D. Mn(II) Binding and Subsequent Oxidation by the Multicopper Oxidase MnxG Investigated by Electron Paramagnetic Resonance Spectroscopy. *J. Am. Chem. Soc.* **2015**, *137* (33), 10563–10575.
- (35) Butterfield, C. N.; Soldatova, A. V.; Lee, S.; Spiro, T. G.; Tebo, B. M. Mn(II,III) Oxidation and MnO₂ Mineralization by an Expressed Bacterial Multicopper Oxidase. *Proc. Natl. Acad. Sci. U. S. A.* 2013, 110 (29), 11731–11735.
- (36) Romano, C. A.; Zhou, M.; Song, Y.; Wysocki, V. H.; Dohnalkova, A. C.; Kovarik, L.; Paša-Tolić, L.; Tebo, B. M. Biogenic Manganese Oxide Nanoparticle Formation by a Multimeric Multicopper Oxidase Mnx. *Nat. Commun.* **2017**, 8 (1), 746 DOI: 10.1038/s41467-017-00896-8.
- (37) Tao, L.; Stich, T. A.; Liou, S. H.; Soldatova, A. V.; Delgadillo, D. A.; Romano, C. A.; Spiro, T. G.; Goodin, D. B.; Tebo, B. M.; Casey, W. H.; Britt, R. D. Copper Binding Sites in the Manganese-Oxidizing Mnx Protein Complex Investigated by Electron Paramagnetic Resonance Spectroscopy. J. Am. Chem. Soc. 2017, 139 (26), 8868—8877.
- (38) Tao, L.; Stich, T. A.; Soldatova, A. V.; Tebo, B. M.; Spiro, T. G.; Casey, W. H.; Britt, R. D. Mn(III) Species Formed by the Multicopper Oxidase MnxG Investigated by Electron Paramagnetic Resonance Spectroscopy. *J. Biol. Inorg. Chem.* **2018**, 23, 1093.
- (39) Soldatova, A. V.; Fu, W.; Romano, C. A.; Tao, L.; Casey, W. H.; Britt, R. D.; Tebo, B. M.; Spiro, T. G. Metallo-Inhibition of Mnx, a Bacterial Manganese Multicopper Oxidase Complex. *J. Inorg. Biochem* **2021**, 224 (June), 111547.
- (40) Tebo, B. M.; Bargar, J. R.; Clement, B. G.; Dick, G. J.; Murray, K. J.; Parker, D.; Verity, R.; Webb, S. M. BIOGENIC MANGANESE OXIDES: Properties and Mechanisms of Formation. *Annu. Rev. Earth Planet Sci.* **2004**, 32 (1), 287–328.
- (41) Simonov, A. N.; Hocking, R. K.; Tao, L.; Gengenbach, T.; Williams, T.; Fang, X. Y.; King, H. J.; Bonke, S. A.; Hoogeveen, D. A.; Romano, C. A.; Tebo, B. M.; Martin, L. L.; Casey, W. H.; Spiccia, L. Tunable Biogenic Manganese Oxides. *Chem. Eur. J.* 2017, 23 (54), 13482–13492, DOI: 10.1002/chem.201702579.
- (42) Namgung, S.; Chon, C.; Lee, G. Formation of Diverse Mn Oxides: A Review of Bio/Geochemical Processes of Mn Oxidation. Geosci. J. 2018, 22 (2), 373–381, DOI: 10.1007/s12303-018-0002-7.
- (43) Pinaud, B. A.; Chen, Z.; Abram, D. N.; Jaramillo, T. F. Thin Films of Sodium Birnessite-Type MnO₂: Optical Properties,

- Electronic Band Structure, and Solar Photoelectrochemistry. J. Phys. Chem. C 2011, 115 (23), 11830–11838.
- (44) Du, X.; Liao, Y.; Ma, M.; Wang, Y.; Zhang, J.; He, G. Advance of Manganese Dioxide-Based Electrocatalyst for Water Splitting. *J. Solid State Chem.* **2024**, 329, 124369.
- (45) Selvakumar, K.; Senthil Kumar, S. M.; Thangamuthu, R.; Kruthika, G.; Murugan, P. Development of Shape-Engineered α -MnO₂ Materials as Bi-Functional Catalysts for Oxygen Evolution Reaction and Oxygen Reduction Reaction in Alkaline Medium. *Int. J. Hydrogen Energy* **2014**, 39 (36), 21024–21036.
- (46) Post, J. E.; Heaney, P. J.; Ilton, E. S.; Elzinga, E. J. The Crystal Structure of Feitknechtite (β -MnOOH) and a New MnOOH Polymorph. *Am. Mineral.* **2023**, 283 (January), 77–80.
- (47) Manceau, A.; Marcus, M. A.; Grangeon, S. Determination of Mn Valence States in Mixed-Valent Manganates by XANES Spectroscopy. *Am. Mineral.* **2012**, *97* (5–6), 816–827.
- (48) Gorlin, Y.; Lassalle-kaiser, B.; Benck, J. D.; Gul, S.; Webb, S. M.; Yachandra, V. K.; Yano, J.; Jaramillo, T. F. In Situ X-Ray Absorption Spectroscopy Investigation of a Bifunctional Manganese Oxide Catalyst with High Activity for Electrochemical Water Oxidation and Oxygen Reduction. J. Am. Chem. Soc. 2013, 135 (23), 8525–8534.
- (49) Junta, J. L.; Hochella, M. F. Manganese (II) Oxidation at Mineral Surfaces: A Microscopic and Spectroscopic Study. *Geochim. Cosmochim. Acta* **1994**, 58 (22), 4985–4999.
- (50) Chan, Z. M.; Kitchaev, D. A.; Weker, J. N.; Schnedermann, C.; Lim, K.; Ceder, G.; Tumas, W.; Toney, M. F.; Nocera, D. G. Electrochemical Trapping of Metastable Mn³⁺ Ions for Activation of MnO₂ Oxygen Evolution Catalysts. *Proc. Natl. Acad. Sci. U. S. A.* **2018**, *115* (23), E5261–E5268.
- (51) Campbell, K. A.; Yikilmaz, E.; Grant, C. V.; Gregor, W.; Miller, A. F.; Britt, R. D. Parallel Polarization EPR Characterization of the Mn(III) Center of Oxidized Manganese Superoxide Dismutase. *J. Am. Chem. Soc.* **1999**, 121 (19), 4714–4715.
- (52) Campbell, K. A. CW and Pulsed EPR Studies of Photosystem II and Mn-Containing Complexes; University of California, 1999.
- (53) Krzystek, J.; Yeagle, G. J.; Park, J.-H.; Britt, R. D.; Meisel, M. W.; Brunel, L.-C.; Telser, J. High-Frequency and -Field EPR Spectroscopy of Tris(2,4-Pentanedionato)Manganese(III): Investigation of Solid-State versus Solution Jahn-Teller Effects. *Inorg. Chem.* 2003, 42 (15), 4610–4618.
- (54) Hendrich, M. P.; Debrunner, P. G. Integer-Spin Electron Paramagnetic Resonance of Iron Proteins. *Biophys. J.* **1989**, *56* (3), 489–506.
- (55) Münck, E.; Ksurerus, K.; Hendrich, M. P. Combining Mössbauer Spectroscopy with Integer Spin Electron Paramagnetic Resonance. *Methods Enzymol.* **1993**, 227 (C), 463–479.
- (56) Jeong, D.; Jin, K.; Jerng, S. E.; Seo, H.; Kim, D.; Nahm, S. H.; Kim, S. H.; Nam, K. T. Mn_5O_8 Nanoparticles as Efficient Water Oxidation Catalysts at Neutral PH. ACS Catal. **2015**, 5 (8), 4624–4628
- (57) Villalobos, M.; Toner, B.; Bargar, J.; Sposito, G.; Illalobos, M. A. V.; Oner, B. R. T.; Argar, J. O. H. N. B.; Posito, G. A. S. Characterization of the Manganese Oxide Produced by Pseudomonas Putida Strain MnB1. *Geochim. Cosmochim. Acta* **2003**, *67* (14), 2649–2662.
- (58) Connor, P.; Schuch, J.; Kaiser, B.; Jaegermann, W. The Determination of Electrochemical Active Surface Area and Specific Capacity Revisited for the System MnO_x as an Oxygen Evolution Catalyst. Z. Physiol. Chem. **2020**, 234 (5), 979–994.
- (59) Wong, J.; Lytle, F. W.; Messmer, R. P.; Maylotte, D. H. K-Edge Absorption Spectra of Selected Vanadium Compounds. *Phys. Rev. B* **1984**, *30* (10), 5596–5610.
- (60) Nealson, K. H.; Ford, J. Surface Enhancement of Bacterial Manganese Oxidation: Implications for Aquatic Environments. *Geomicrobiol. J.* **1980**, 2 (1), 21–37.
- (61) Francis, C. A.; Tebo, B. M. Marine Bacillus Spores as Catalysts for Oxidative Precipitation and Sorption of Metals. *J. Mol. Microbiol. Biotechnol.* **1999**, *1* (1), 71–78.

- (62) Oku, M.; Hirokawa, K.; Ikeda, S. X-Ray Photoelectron Spectroscopy of Manganese-Oxygen Systems. *J. Electron Spectrosc. Relat. Phenom.* **1975**, 7 (5), 465–473.
- (63) Foord, J. S.; Jackman, R. B.; Allen, G. C. An X-Ray Photoelectron Spectroscopic Investigation of the Oxidation of Manganese. *Philos. Mag. A* **1984**, 49 (5), 657–663.
- (64) Carver, J. C.; Schweitzer, G. K.; Carlson, T. A. Use of X-Ray Photoelectron Spectroscopy to Study Bonding in Cr, Mn, Fe, and Co Compounds. *J. Chem. Phys.* **1972**, *57* (2), 973–982.
- (65) Nelson, A. J.; Reynolds, J. G.; Roos, J. W. Core-Level Satellites and Outer Core-Level Multiplet Splitting in Mn Model Compounds. *J. Vac. Sci. Technol., A* **2000**, *18* (4), 1072–1076.
- (66) Gorlin, Y.; Jaramillo, T. F. A Bifunctional Nonprecious Metal Catalyst for Oxygen Reduction and Water Oxidation. *J. Am. Chem. Soc.* **2010**, *132* (39), *13612–13614*.
- (67) Gorlin, Y.; Lassalle-Kaiser, B.; Benck, J. D.; Gul, S.; Webb, S. M.; Yachandra, V. K.; Yano, J.; Jaramillo, T. F. In Situ X-Ray Absorption Spectroscopy Investigation of a Bifunctional Manganese Oxide Catalyst with High Activity for Electrochemical Water Oxidation and Oxygen Reduction. J. Am. Chem. Soc. 2013, 135 (23), 8525–8534.
- (68) Ilton, E. S.; Post, J. E.; Heaney, P. J.; Ling, F. T.; Kerisit, S. N. XPS Determination of Mn Oxidation States in Mn (Hydr)Oxides. *Appl. Surf. Sci.* **2016**, *366*, 475–485.
- (69) Cerrato, J. M.; Hochella, M. F.; Knocke, W. R.; Dietrich, A. M.; Cromer, T. F. Use of XPS to Identify the Oxidation State of Mn in Solid Surfaces of Filtration Media Oxide Samples from Drinking Water Treatment Plants. *Environ. Sci. Technol.* **2010**, 44 (15), 5881–5886
- (70) Galakhov, V. R.; Demeter, M.; Bartkowski, S.; Neumann, M.; Ovechkina, N. A.; Kurmaev, E. Z.; Lobachevskaya, N. I.; Mukovskii, Y. M.; Mitchell, J.; Ederer, D. L. Mn Exchange Splitting in Mixed-Valence Manganites. *Phys. Rev. B: Condens. Matter Mater. Phys.* **2002**, 65 (11), 113102 DOI: 10.1103/PhysRevB.65.113102.
- (71) Lee, J. H.; Sa, Y. J.; Kim, T. K.; Moon, H. R.; Joo, S. H. A Transformative Route to Nanoporous Manganese Oxides of Controlled Oxidation States with Identical Textural Properties. *J. Mater. Chem. A: Mater.* **2014**, 2 (27), 10435–10443.
- (72) Murray, J. W.; Dillard, J. G.; Giovanoli, R.; Moers, H.; Stumm, W. Oxidation of Mn(II): Initial Mineralogy, Oxidation State and Ageing. *Geochim. Cosmochim. Acta* 1985, 49 (2), 463–470.
- (73) Han, X.; Cui, Y.; Liu, H. Ce-Doped Mn₃O₄ as High-Performance Anode Material for Lithium Ion Batteries. *J. Alloys Compd.* **2020**, *814*, 152348.
- (74) Sun, M.; Lan, B.; Lin, T.; Cheng, G.; Ye, F.; Yu, L.; Cheng, X.; Zheng, X. Controlled Synthesis of Nanostructured Manganese Oxide: Crystalline Evolution and Catalytic Activities. *CrystEngComm* **2013**, *15* (35), 7010–7018.
- (75) Li, J. Y.; Wu, X. L.; Zhang, X. H.; Lü, H. Y.; Wang, G.; Guo, J. Z.; Wan, F.; Wang, R. S. Romanechite-Structured Na_{0.31}MnO_{1.9} Nanofibers as High-Performance Cathode Material for a Sodium-Ion Battery. *Chem. Commun.* **2015**, *51* (80), 14848–14851.